



Cite this: DOI: 10.1039/c9cp06821j

# Aqueous solvation of the chloride ion revisited with density functional theory: impact of correlation and exchange approximations†

Mark DelloStritto,<sup>ID \*a</sup> Jianhang Xu,<sup>b</sup> Xifan Wu<sup>b</sup> and Michael L. Klein<sup>a</sup>

The specificity of aqueous halide solvation is fundamental to a wide range of bulk and interfacial phenomena spanning from biology to materials science. Halide polarizability is thought to drive the ion specificity, and if so, it is essential to have an accurate description of the electronic properties of halide ions in water. To this end, the solvation of the chloride anion,  $\text{Cl}^-$  has been reinvestigated with state-of-the-art density functional theory. Specifically, the PBE-D3, PBE0-D3, and SCAN functionals have been employed to probe the impact of correlation and exchange approximations. Anticipating the findings, adding exact exchange improves the electronic structure, but simultaneously significantly reduces the  $\text{Cl}^-$  polarizability, resulting in an over-structured Cl–O radial distribution function (RDF) and longer water H-bond lifetimes to  $\text{Cl}^-$ . SCAN does not yield as much improvement in the energetics of  $\text{Cl}^-$  relative to bulk water, but does result in a smaller reduction of the polarizability and thus a less structured Cl–O RDF, which agrees better with experiment. Special consideration is therefore warranted in assessing the impact of exchange on the energy, charge density, and the charge density response when designing and testing hybrid functionals for aqueous halide solvation.

Received 18th December 2019,  
Accepted 27th January 2020

DOI: 10.1039/c9cp06821j

rsc.li/pccp

## 1 Introduction

The nature of the solvation of ions in water is an important field of study with an enormous range of applications. The role of ions in biological systems has been recognized for well over a century, beginning with the discovery of the Hofmeister series<sup>1</sup> for proteins and extending to a wide variety of systems.<sup>2–4</sup> Ion solvation also plays an important role in geoscience and environmental chemistry, where ions display specific adsorption at aqueous interfaces,<sup>5,6</sup> driving dissolution behavior of oxide minerals<sup>7,8</sup> as well as playing an important role in the structure of sea spray aerosols,<sup>9,10</sup> which impact ice nucleation and radiative forcing.<sup>11,12</sup> Solvated ions play an important role in batteries<sup>13</sup> and catalysis in both biological<sup>14</sup> and artificial systems<sup>15,16</sup> as well. In all of these applications, it is essential to understand the specific nature of the ion and how it interacts with  $\text{H}_2\text{O}$  molecules, aqueous interfaces, and other molecules. It is therefore paramount that one has highly accurate models of ion–water interactions, which yield not only the correct

structural, electronic, and optical properties of the hydrated ions, but the correct dynamical properties as well.

Halide ions display specific ion phenomena. The oldest and most famous is the Hofmeister series, where it was found that the ability of halides to precipitate egg white protein follows the behavior:<sup>1</sup>  $\text{Cl}^- > \text{Br}^- > \text{I}^-$ . Similar trends in the halides were found in their affinity for the air/water and hydrophobic interfaces, with larger, more polarizable halides displaying greater propensity for the surface.<sup>5,17,18</sup> The opposite can be found at hydrophilic interfaces, where sum frequency generation experiments show that smaller, less polarizable ions like  $\text{F}^-$  have a greater impact on the intensity and therefore are inferred to have a greater surface affinity.<sup>19</sup> The Hofmeister series is also found in bulk solutions *via* the impact of halides on Raman spectra<sup>20</sup> and the viscosity.<sup>21</sup> Taken together, these data have lead to the classification of ions as either “structure-makers” (cosmotropes) or “structure-breakers” (kaotropes), with smaller, less polarizable ions increasing the structure of nearby water molecules and larger, more polarizable ions decreasing the local structure. Simple classical models of halide solvation are inadequate to explain these observations, which require an accurate description of the electronic structure of halide ions in water, and in particular an accurate model of halide polarizabilities. Indeed, polarizable force fields generally yield significantly more accurate results for halides when compare to non-polarizable force fields,<sup>22–24</sup> correctly predicting the affinity of  $\text{Cl}^-$  for “surface” structures in small water clusters.<sup>24–27</sup>

<sup>a</sup> Institute for Computational Molecular Science, Temple University SERC, Philadelphia, 1925, N 12th St, PA 19122, USA.

E-mail: mark.dellostritto@temple.edu

<sup>b</sup> Department of Physics, Temple University SERC, 1925, N 12th St, Philadelphia, PA 19122, USA

† Electronic supplementary information (ESI) available: Radial, angular, and velocity distributions of water molecules. See DOI: 10.1039/c9cp06821j

The complex electronic structure of halide–water interactions presents significant challenges for modeling and simulation. While polarizable force fields generally yield accurate structures for halide ions, they have a limited range of accuracy and generally cannot be used to study electronic properties. Bulk solvation is typically studied with density functional theory (DFT) and a periodic system containing one ion plus at least 63H<sub>2</sub>O molecules,<sup>28,29</sup> as the high level quantum chemistry methods appropriate for small halide–water clusters are prohibitively expensive. The use of DFT presents its own set of challenges, as LDA and GGA functional generally do not yield accurate halide polarizabilities due to self-interaction errors. Thus, it is often necessary to use expensive hybrid functionals, which include a portion of exact exchange to yield accurate polarizabilities from DFT.<sup>30</sup> However, although hybrid functionals include exact exchange, the percentage is an empirical parameter and can still fail for systems where electron correlation is important, *e.g.* strongly correlated systems. Meta-GGA functionals include a dependence of the energy of the kinetic energy density and thereby reduce the delocalization error, allowing meta-GGAs like SCAN<sup>31</sup> to yield much more accurate results for a wide range of systems.<sup>32</sup> Recent energy decomposition analysis calculations of small halide–water clusters show that several popular GGA, hybrid, and meta-GGA functionals can differ strongly in the predicted energies, especially for the energy associated with Pauli repulsion and London dispersion, emphasizing the importance of many-body effects and the details of the chosen functional.<sup>33,34</sup> In bulk solutions, these discrepancies can lead to significant differences in the solvation structure and electronic properties.<sup>28,35</sup> Discrepancies between models can help drive controversy in the community over *e.g.* the extent to which halides modify the structure of the surrounding H<sub>2</sub>O molecules.<sup>36–42</sup> Thus, it is important to properly characterize the impact of different functionals on halide solvation. Specifically, the effects on the solvation structure and polarizability, and how the properties of the system correlate with the accuracy of the exchange and correlation energy approximations.

Ab initio molecular dynamics (AIMD) simulations have been performed on a periodically replicated system of one Cl<sup>−</sup> solvated by 63H<sub>2</sub>O molecules in order to study the solvation structure, the H-bond dynamics, and the polarizability and charge distribution of the Cl<sup>−</sup> ion. The PBE-D3, PBE0-D3, and SCAN functionals have been employed in order to compare different approximations of the exchange and correlation energies. The SCAN meta-GGA functional is known to yield excellent results for water,<sup>43</sup> hydrophilic interfaces,<sup>16</sup> and the solvation of alkali ions.<sup>44</sup> Recent benchmark calculations show that SCAN yields errors of ~2 kcal mol<sup>−1</sup> for Cl<sup>−</sup>–(H<sub>2</sub>O)<sub>2</sub> clusters, compared to errors of ~0 kcal mol<sup>−1</sup> PBE, PBE0, and ωB97M-V functionals.<sup>25</sup> Nevertheless, the SCAN functional has been employed here due to its excellent accuracy for water in a wide range of environments. Moreover, the accuracy of a functional for isolated clusters may not necessarily hold in bulk due to changes in structure and charge density upon complete solvation.<sup>26</sup> We have chosen not to use SCAN-D3 or the hybrid functional SCAN0 as adding vdW corrections leads to large

negative pressures in liquid water,<sup>45</sup> while adding exact exchange to SCAN does not lead to an improvement in accuracy in all cases.<sup>46</sup>

To address the above issues, here Cl<sup>−</sup> solvation is investigated using state of the art density functional approximations, including a range of correlation approximations and exact exchange fractions. It is found that the choice of functional has a strong impact on both the solvation structure of the Cl<sup>−</sup> as well as the electronic properties of the system. While both the meta-GGA functional SCAN and hybrid GGA functional PBE0-D3 soften the Cl–O RDF with respect to PBE-D3, in agreement with experiment,<sup>37,47</sup> SCAN yields a solvation structure that is closest to experimental values. The PBE0-D3 yields a slightly more structured Cl<sup>−</sup> solvation shell compared to SCAN because the addition of exact exchange leads to a large reduction in the Cl<sup>−</sup> polarizability, thereby leading to longer H-bond lifetimes and a more rigid solvation environment. By systematically varying the exact exchange fraction and density functional, it is found that the Cl<sup>−</sup> polarizability strongly depends on the exact exchange fraction for hybrid PBE. It is also found that this dependence on the exact exchange fraction is reduced in hybrid SCAN, and that the reduction in the Cl<sup>−</sup> polarizability when moving from PBE to SCAN is much less than when moving from PBE to PBE0. On the other hand, PBE0-D3 is the only functional to yield a Cl<sup>−</sup>(3p) band above the VBM of water in the density of states in a manner that is qualitatively consistent with photoelectron spectroscopy experiments,<sup>48</sup> though SCAN does improve the separation of the Cl<sup>−</sup>(3p) and VBM of water compared to PBE. Thus, while the exact exchange term of hybrid GGAs can improve the accuracy of the functional by reducing the self-interaction error, it can also yield incorrect results for properties such as the polarizability due to the empirical nature of the exact exchange fraction.

## 2 Computational methods

MD simulations were carried out on periodically replicated systems of a single Cl<sup>−</sup> solvated by 63H<sub>2</sub>O molecules in either the *NVT* or *NVE* ensembles at a temperature of 330 K. An elevated temperature was used in order to mimic the effects of nuclear quantum effects on the structure of the water solvent. A cubic simulation cell with box edge length 12.518 Å yielded a density of 0.998 g cm<sup>−3</sup>. The AIMD calculations were initialized with configurations taken from classical MD simulations that employed the SPC/E water intermolecular potential<sup>49</sup> plus a Cl<sup>−</sup> ion–water potential<sup>47</sup> using the LAMMPS package.<sup>50</sup> The MD simulations were run for 2 ns in the *NVT* ensemble to equilibrate the random initial configurations which were generated with PACKMOL.<sup>51</sup> All subsequent molecular dynamics calculations (MD) are run using CP2K v.5.1.<sup>52</sup> Three different simulations of Cl<sup>−</sup> in water were run with three different functionals: PBE<sup>53,54</sup> with the Grimme D3 vdW correction<sup>55–57</sup> (PBE-D3), PBE0<sup>58</sup> with the D3 correction (PBE0-D3), and SCAN.<sup>31</sup> For all atoms the GTH pseudopotentials<sup>59</sup> are used with the MOLOPT<sup>60</sup> split valence triple zeta basis sets. A plane-wave cutoff of 500 Ry is used for

the PBE-D3 and PBE0-D3 simulations, while for the SCAN simulations a cutoff of 1200 Ry is used in order to obtain accurate forces.<sup>61,62</sup> The Quickstep module of CP2K is used to run the molecular dynamics simulations with a timestep of 0.5 fs. Wannier functions were computed every 5 timesteps (2.5 fs) and the Wannier centers and spreads were saved to file. In order to improve the efficiency of the hybrid simulations, the auxiliary density matrix method<sup>63</sup> with the cpFIT3 basis as the auxiliary basis, and a truncated Coulomb operator was used with a cutoff radius of 6.0 Å in order to prevent self-exchange interactions. For the density of states calculations Quantum Espresso v.6.3<sup>64,65</sup> was used with the HSCV pseudopotentials,<sup>66</sup> a cutoff of 95 Ry for the PBE-D3 and PBE0-D3 calculations, and a cutoff of 130 Ry for the SCAN calculations. Quantum Espresso was also used for initial Born–Oppenheimer MD simulations of Cl<sup>−</sup> solvated by 63H<sub>2</sub>O molecules using the SCAN functional with a cutoff of 85 Ry at 300K using the cp module in order to test the performance of SCAN for Cl<sup>−</sup> solvation.

AIMD simulations were first initialized from the last frame of the classical MD simulations, and were then run in the *NVT* ensemble with the PBE-D3 functional for 1 ps. The last frame of this first AIMD simulation was then taken as the initial configuration for all subsequent AIMD simulations. Each different simulation for each functional was then run in the *NVT* ensemble using a Nose–Hoover thermostat at 330 K until the total energy of the system appeared to stop changing (around 2–3 ps) followed by simulations run in the *NVE* ensemble. Each simulation was run for at least 16 ps in order to compute the structural and electronic properties of the solvated Cl<sup>−</sup> ion. The density of states (DOS) of the system was sampled every 0.125 ps, and the Hirshfeld-I<sup>67,68</sup> charges and the static polarizabilities of the Cl<sup>−</sup> and H<sub>2</sub>O were sampled every 0.5 ps. The Cl<sup>−</sup> polarizability is computed by applying electric fields of intensity ±0.0025 a.u. in the *x*, *y*, and *z* directions, computing the dipole of the ion/molecule at each point, and finally taking the gradient with respect to the electric field.

### 3 Results and discussion

The structure of solvated Cl<sup>−</sup> was characterized by the distribution of distances, angles, and coordination numbers. An AIMD simulation was run using Quantum Espresso (QE) at 300K for 50 ps in order to obtain well-converged Cl–O and Cl–H radial distribution functions (RDFs) shown in Fig. 2, which is compared to AIMD simulations of the same system run at 330 K using CP2K for 16 ps. While the RDFs from the 300 K simulation closely match the experimental data, they are slightly overstructured, likely due to the absence of nuclear quantum effects (NQE). The 330 K SCAN simulation on the other hand yields a second solvation shell of the Cl–O RDF which better matches experiment, while the first peak associated with the first solvation shell is slightly lower than experiment. One can see similar effects of the temperature on the Cl–H RDF, with an increase in the temperature improving the second solvation shell while reducing agreement with experiment for the first

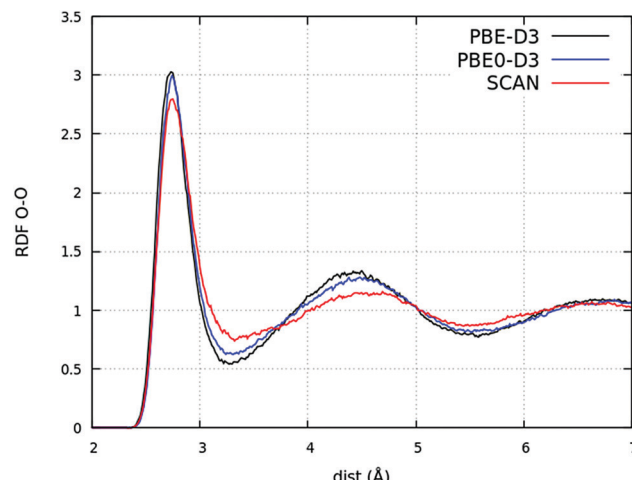


Fig. 1 The O–O radial distribution function for the simulations performed with CP2K at 330 K.

solvation shell. Running the simulations at 330 K does therefore improve the solvation structure, but cannot completely correct for the absence of NQE, as evidenced by the obvious discrepancy in the Cl–H RDF.

In order to compare different functionals, MD simulations were performed with the PBE-D3, PBE0-D3, and SCAN functionals using CP2K at 330 K to roughly mimic the impact of NQE on the water structure,<sup>69</sup> and CP2K is preferred because it allows us to efficiently compute Wannier functions during the MD simulation. Notably, the PBE-D3, PBE0-D3, and SCAN functionals all yield O–O RDFs which are in good agreement with experiment, with the PBE0-D3 functional yielding slightly less structured water compared to PBE-D3, and SCAN yielding slightly less structured water compared to PBE0-D3 (Fig. 1). While the differences in the O–O RDF are slight, the differences in the O–O–O angular distribution function (ADF) are more pronounced, with SCAN yielding a broader distribution, especially at smaller angles, indicative of the shorter H-bond lifetimes and less structured nature of SCAN water.<sup>43</sup> These results are mirrored in the Cl–O and Cl–H RDFs in Fig. 3. Notably, while all functionals yield similar peak positions (Table 1), PBE0-D3 yields a less structured Cl–O RDF compared to PBE-D3, and SCAN yields a much less structured RDF, with a very broad peak at around 5 Å which is difficult to distinguish. Moreover, the SCAN Cl–O RDF best reproduces experimental results, which show that Cl<sup>−</sup> has an RDF with very little structure,<sup>37,47</sup> with the elevated temperature improving the agreement beyond the first solvation shell. The experimentally measured Cl–O RDF

Table 1 Peak and minimum positions in the Cl–O RDF (Å) as shown in Fig. 3

Functional	$r_{\max}^{(1)}$	$r_{\min}^{(1)}$	$r_{\max}^{(2)}$	$r_{\min}^{(2)}$
PBE-D3	3.14	3.78	4.85	6.10
PBE0-D3	3.17	3.85	5.15	5.90
SCAN	3.17	3.85	4.90	5.90
Expt. <sup>37</sup>	3.14	3.77	4.99	6.19

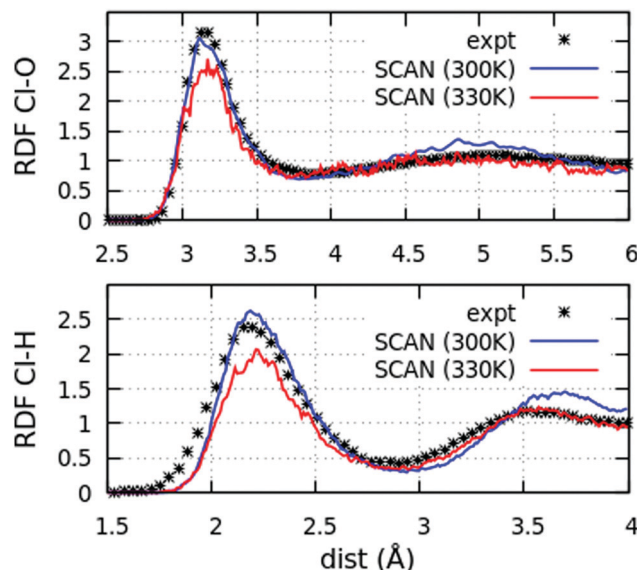


**Fig. 2** The radial distribution function for Cl–O (top) and Cl–H (bottom). The SCAN (300 K) simulations are performed with QE while the SCAN (330 K) simulations are performed with CP2K, and the experimental RDF is inferred using empirical potential structure refinement from neutron diffraction data.<sup>37</sup>

is similar to that of  $\text{Br}^-$  and  $\text{I}^-$ , with  $\text{I}^-$  having no second maximum at all, while it differs from the F–O RDF which is much more structured. These findings are consistent with the determination that  $\text{Cl}^-$ ,  $\text{Br}^-$ , and  $\text{I}^-$  are structure-breaking ions while  $\text{F}^-$  is structure-making.<sup>70</sup> While the Cl–H RDF does not show as much difference between the functionals as the Cl–O RDF, note that SCAN shows better agreement with experiment at the first minimum, and is indicative of a more disordered solvation shell.

Further evidence of the disordered nature of the  $\text{Cl}^-$  solvation shell in the SCAN simulation can be seen in the  $\text{Cl}^-$  coordination number (CN) and the O–Cl–O ADF. The distributions of  $\text{Cl}^-$  CNs for each functional are shown in Fig. 4, which displays the number of neighbors up to the first minimum in the Cl–O RDF. The SCAN functional has a much broader distribution compared to the GGA functionals and is shifted to larger CNs, with short-lived states with up to 12 neighbors that are likely due to exchange events. The PBE0-D3 functional on the other hand has a narrower distribution of coordination numbers compared to the PBE-D3 functional, despite the fact that the PBE0-D3 Cl–O RDF is less structured than that of PBE-D3. This suggests that PBE0-D3 predicts weaker H-bonds with shorter lifetimes compared to PBE-D3, but predicts a more rigid solvation shell with fewer exchange events. Meanwhile, the SCAN simulations suggest a much less structured solvation shell with a greater frequency of exchange events. Further evidence of a more disordered  $\text{Cl}^-$  solvation shell is revealed in the O–Cl–O ADF in Fig. 5, which shows that the SCAN ADF is broader than the GGA functionals, with much greater amplitudes between  $40^\circ$  and  $60^\circ$ . This region of the ADF in the O–O–O distribution is associated with  $\text{H}_2\text{O}$  molecules with 0–1 H-bonds,<sup>43</sup> and so the increase in the ADF in this region indicates that the

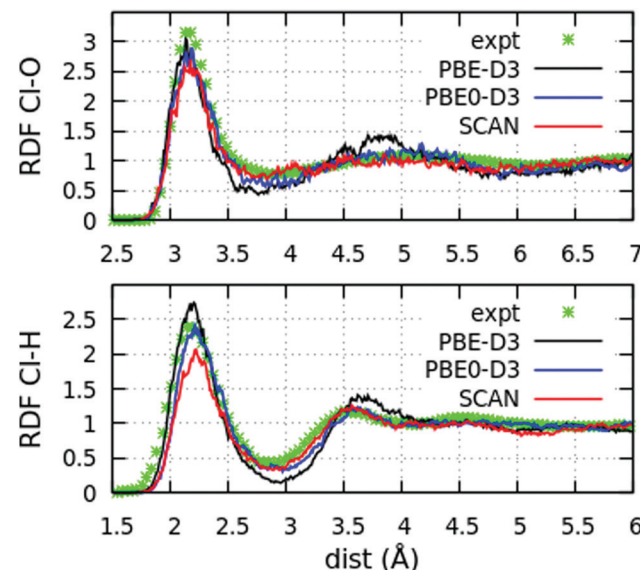


**Fig. 3** The radial distribution function for Cl–O (top) and Cl–H (bottom). The simulations are performed with CP2K at 330 K and the experimental RDF is inferred using empirical potential structure refinement from neutron diffraction data.<sup>37</sup>

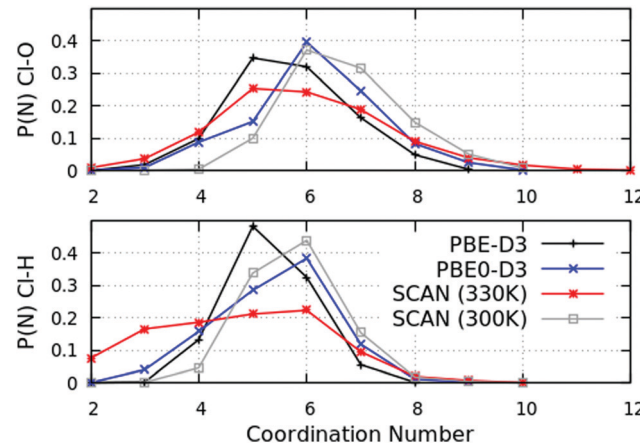


**Fig. 4** The distribution of the Cl–O (top) and Cl–H (bottom) coordination numbers computed by counting the number of neighbors up to the first minimum in the Cl–O and Cl–H RDF, respectively. The SCAN (300 K) simulations are performed with QE, while all others are performed with CP2K at 330 K.

water–Cl H-bonds are more likely to break and leave the  $\text{Cl}^-$  H-bond deficient. Finally, by comparing to the simulations of  $\text{Cl}^-$  run with SCAN using QE at 300 K, one sees that the temperature of the simulation has a large impact on the solvation structure, particularly by increasing the incidence of configurations with few H-bonds to  $\text{Cl}^-$ . This highlights the importance of nuclear quantum effects when modeling ion solvation, though such considerations are beyond the scope of this paper.

In order to gain a deeper understanding of the  $\text{Cl}^-$  solvation shell and its relation to the local H-bond network, the H-bond lifetime and number of H-bonds, defined as total number of H-bonds of each  $\text{H}_2\text{O}$  molecule or  $\text{Cl}^-$ , was computed for each

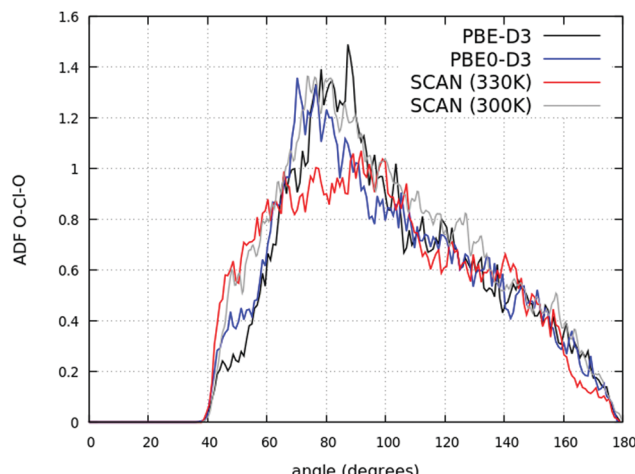


**Fig. 5** The angular distribution function of the O–Cl–O angles (Cl pivot point) for all O atoms within the first minimum of the Cl–O RDF (3.85 Å). The SCAN (300 K) simulations are performed with QE, while all others are performed with CP2K at 330 K.

simulation. The standard geometric definition of a H-bond was employed, where a H-bond exists if the distance between the donor O (Od) and the acceptor O (Oa) is within the first minimum of the O–O RDF (3.25 Å) and if the H–Od–Oa angle is within 30°. The H-bond from a H<sub>2</sub>O molecule to Cl<sup>−</sup> is defined to exist if the Od–Cl<sup>−</sup> distance is within the first minimum of the Cl–O RDF (3.80 Å) and the H–Od–Cl angle is within 30, as the H–Od–Cl angle within this cutoff has a very similar distribution to H–Od–Oa angles Fig. 6.

The average H-bond lifetime and average number of H-bonds of each molecule and Cl<sup>−</sup> are given in Table 2. As expected from the O–O–O ADF,<sup>43</sup> as one goes from PBE-D3 to PBE0-D3 to SCAN, the H<sub>2</sub>O H-bond lifetime and number decrease, as SCAN yields a greater incidence of H<sub>2</sub>O molecules with 0–1 H-bonds. While adding exact exchange to the PBE-D3 functional does yield shorter H-bond lifetimes, they are still

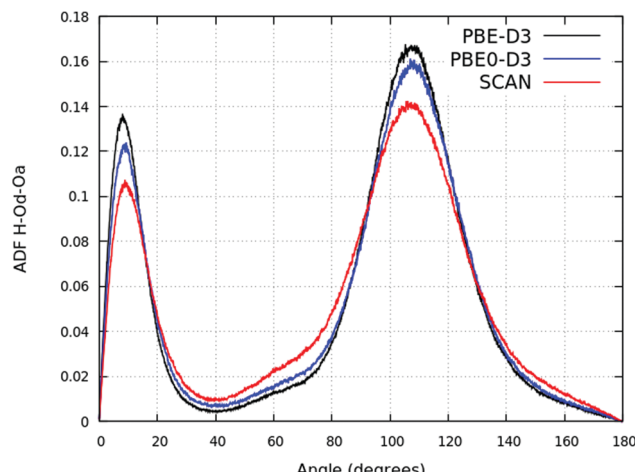


**Fig. 6** The angular distribution function of the H–Od–Oa angles (Od pivot point) where we use a cutoff of 3.35 Å for the O–O distance and a cutoff of 1.2 Å for the O–H distance.

**Table 2** H-Bond lifetime and average H-bond number computed from AIMD trajectories with various functional approximations

Functional	O	Cl
H-Bond life times (fs)		
PBE-D3	393	264
PBE0-D3	285	188
SCAN	210	141
Functional		
Number of H-bonds		
PBE-D3	3.60	4.89
PBE0-D3	3.59	4.88
SCAN	3.41	4.61

significantly longer than the SCAN lifetimes. These results help explain the differences between the functionals in the Cl–O RDF, Cl–O CN, and O–Cl–O ADF. When exact exchange is added to the PBE-D3 functional to get PBE0-D3, there is a decrease in the overall water structure and a decrease in the H-bond lifetimes, leading to a slight softening of the O–O RDF. The change in H-bond lifetime is much less pronounced for the Cl<sup>−</sup> however, which is why the distribution of CNs is so sharply peaked for PBE0-D3 and why the O–Cl–O ADF for PBE-D3 and PBE0-D3 are so similar. On the other hand, the SCAN functional leads to a large reduction of H-bond lifetimes for both H<sub>2</sub>O and Cl<sup>−</sup>, leading to a softening of both the O–O and Cl–O RDFs as well as a broader distribution of Cl<sup>−</sup> coordination numbers.

The electronic properties of the chloride simulations were investigated in order to understand how the differences in solvation structure and dynamics are related to the differences in the functionals. The density of states (DOS) and projected DOS for Cl<sup>−</sup> are sampled every 0.125 ps for each simulation, using the same functional that is used for the AIMD simulation, and is shown in Fig. 7 with the CBM placed at the origin. Each DOS shows four main peaks due to H<sub>2</sub>O, the lowest is

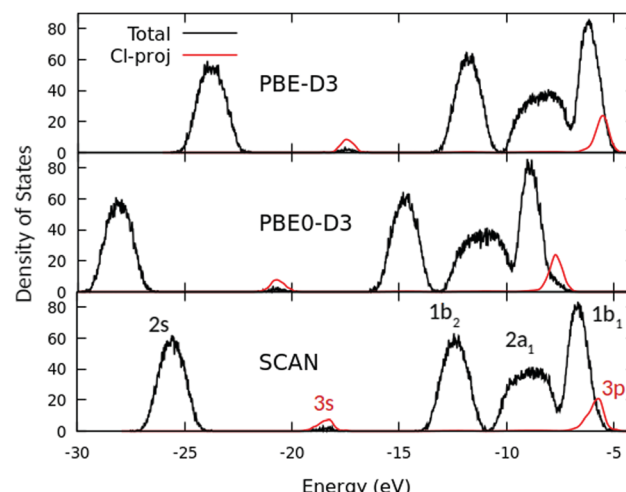


**Fig. 7** The electronic density of states (black) and Cl<sup>−</sup> projected density of states (red) sampled every 0.125 fs from each simulation and smoothed with a Gaussian with a width of 0.15 eV. The Cl<sup>−</sup> projected density of states has been multiplied by 5 to make it more visible.

**Table 3** The energy difference  $\delta E$  between the peaks of the  $1b_1$  peak of bulk water and the  $3p$  state of the solvated  $\text{Cl}^-$  ion

	O $1b_1$ (eV)	Cl $3p$ (eV)	$\delta E$ (eV)
Expt. <sup>48</sup>	-11.31	-9.6	1.71
PBE-D3	-6.13	-5.49	0.64
PBE0-D3	-8.90	-7.67	1.23
SCAN	-6.68	-5.69	0.99

associated with the  $2s$  orbital of O while the three peaks in the upper valence region are associated with the  $1b_2$ ,  $3a_1$ , and  $1b_1$  orbitals.<sup>71</sup> The  $3s$  band of  $\text{Cl}^-$  is situated between the  $2s$  and  $1b_2$  bands of  $\text{H}_2\text{O}$ , while the  $3p$  band of  $\text{Cl}^-$  is close to the VBM of  $\text{H}_2\text{O}$ . Both PBE0-D3 and SCAN lead to a shift in the VBM to lower energies and a relative shift of the  $3p$  band of  $\text{Cl}^-$  to higher energies. While PBE0-D3 shows the  $3p$  band above the VBM of water as expected,<sup>72</sup> the  $3p$  band in the SCAN simulation is not completely above the VBM, although its position is improved with respect to PBE-D3. This analysis is made more concrete by listing the positions of the O( $1b_1$ ) and  $\text{Cl}^-$ ( $3p$ ) peaks and their difference compared with experiment<sup>48</sup> in Table 3. Once again, PBE0-D3 yields the results closest to experiment, shifting the difference between the O( $1b_1$ ) and  $\text{Cl}^-$ ( $3p$ ) peaks ( $\delta E$ ) to greater values. Meanwhile, SCAN improves the value of  $\delta E$  relative to PBE-D3, but does not yield as accurate results as PBE0-D3. Previous results have shown that the DOS depends both upon the density functional approximation as well as the  $\text{Cl}^-$  solvation structure,<sup>28</sup> with shifts in the Cl-O and Cl-H RDFs to slightly larger distances resulting in less favorable hybridisation between the Cl( $3p$ ) and O( $2p$ ) orbitals. The improvement in the  $\delta E$  yielded by SCAN is therefore likely due to improvements in the self-interaction error<sup>32</sup> which impacts Cl-O hybridization directly<sup>28,35</sup> and due to improvements in the accuracy of the  $\text{Cl}^-$  solvation structure.

When it comes to solvation however, often the more important quantities are the local charge and response of the halide ion, as the Hofmeister series appears to imply that the size and polarizability of halide ions is what drives ion specificity.<sup>2</sup> With this in mind, the polarizability of the  $\text{Cl}^-$  ion was computed in each simulation. There are two approaches one can take to computing the polarizability: the first is to compute a static polarizability by applying an electric field and measuring the response of the charge density *via* the shift in the Wannier center positions. Note that this method slightly underestimates the polarizability by disregarding the shape of the Wannier functions, but should provide a good comparison between functionals.<sup>73</sup> Alternatively, one can instead measure the fluctuation of the Wannier centers over time and extract a frequency dependent response:

$$\alpha(\omega) = \frac{2\pi\omega^2\beta}{3cV\eta(\omega)} \int_{-\infty}^{\infty} \langle \mu(t)\mu(0) \rangle e^{i\omega t} dt \quad (1)$$

where  $\beta$  is the inverse temperature,  $c$  is the speed of light, and  $\eta(\omega)$  is the index of refraction, which is multiplied out in order to get a quantity which is directly proportional to the polarizability.<sup>74</sup> This quantity, if computed using the dipole

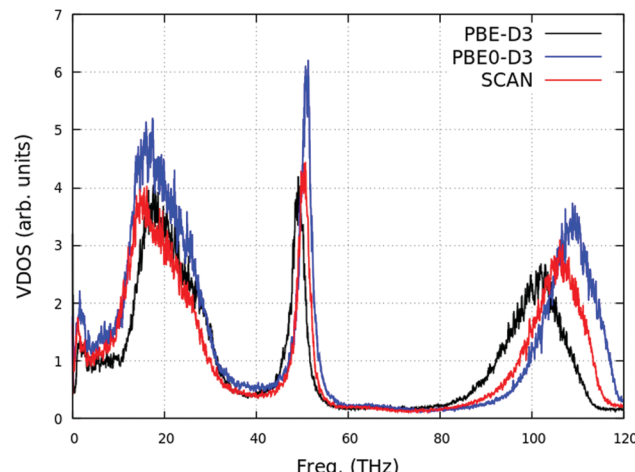


**Fig. 8** The vibrational density of states (VDOS) of the H atoms for each simulation. The VDOS has been windowed using a Blackman–Harris function<sup>75</sup> and smoothed with a Gaussian with a width of 15 fs.

moment of the  $\text{Cl}^-$  only, will not yield the intrinsic polarizability of  $\text{Cl}^-$  as the adsorption coefficient must go to zero as the frequency goes to zero. Nevertheless,  $\alpha(\omega)$  does give us the response of the dipole moment of  $\text{Cl}^-$  to perturbations due to solvent fluctuations as a function of frequency, which should depend sensitively on the underlying electronic structure of the solvated ion.

The quantity  $\alpha(\omega)$  is plotted in Fig. 9 where significant differences are revealed between the adsorption coefficients of different functionals. The difference in the positions of the peaks in  $\alpha(\omega)$  between each functional is easily explained by the differences in the vibrational density of states between each functional (Fig. 8). Adding exact exchange to PBE significantly blue-shifts the O-H stretching peak at ~100 THz while switching from PBE to SCAN yields a lesser blue-shift. The different intensities meanwhile correspond to the response of charge density of the  $\text{Cl}^-$  ion to perturbations due to H-bonding and the local potentials of nearest neighbor  $\text{H}_2\text{O}$  molecules. As one moves from PBE-D3 to PBE0-D3 to SCAN, the response of the  $\text{Cl}^-$  is significantly reduced, especially in the OH-stretching region. This indicates that the polarizability of the  $\text{Cl}^-$  is reduced in the PBE0-D3 simulation, as eqn (1) shows that the intensity of  $\alpha(\omega)$  is proportional to the magnitude of the fluctuations of the  $\text{Cl}^-$  dipole moment.

In addition to computing  $\alpha(\omega)$ , the static polarizability and charge state of the  $\text{Cl}^-$  were evaluated every 0.5 ps in order to better understand how they differ with the choice of functional. Specifically, trajectories were sampled every 0.5 ps and the polarizability and Hirshfeld-I charge of  $\text{Cl}^-$  were computed using the Perdew–Zunger<sup>76</sup> (PZ), PBE, and SCAN functionals with exact exchange fractions of {0.00, 0.05, 0.10, 0.15, 0.20, 0.25}. Trajectories are sampled from the SCAN simulation at 330 K only, computing the polarizability with each functional and exact exchange fraction for each frame, in order to provide a more direct comparison. This procedure allows one to fully understand how the polarizability and charge are determined

by the exchange and correlation approximations employed. At each frame one can freely change the fraction of exact exchange for each functional, and one can move from LDA to GGA to meta-GGA approximations of the exchange correlation potential as one goes from PZ to PBE to SCAN. This then gives a rough approximation of the polarizability as a function of the accuracy of the correlation and exchange energies without making use of more complex energy decomposition analyses. The average polarizability and Hirshfeld-I charge of the  $\text{Cl}^-$  as a function of the functional is listed in Table 4. As expected, going from PZ to PBE one sees a large change in the polarizability and charge, while when going from PBE to SCAN the change is much smaller. In addition, although the charge does not change much as a function of exact exchange fraction, the polarizability decreases by a large percentage as one goes from 0.00 to 0.25 fraction of exact exchange. This observation is consistent with the fact that local and semi-local DFT functionals generally over-estimate the delocalization of electrons due to self-interaction errors.

The choice of density functional approximation has a large impact on the  $\text{Cl}^-$  polarizability, and thereby a large impact on its solvation environment. Unfortunately, it is difficult to know what the “correct” value of the polarizability should be, as these calculations are impacted by finite size effects, which reduce the value of the polarizability compared to infinite dilution.<sup>73</sup> However, larger scale calculations have shown that the polarizability of solvated  $\text{Cl}^-$  in the limit of infinite dilution is nearly equal to its gas phase value.<sup>73</sup> Thus, one should not expect large reductions of the  $\text{Cl}^-$  polarizability upon solvation. Even though moving from PBE to SCAN results in a reduction in the  $\text{Cl}^-$  polarizability, one sees a much greater reduction when adding 0.25 exact exchange to PBE. Thus, it appears that the inability of PBE0-D3 to significantly improve the structure of solvated  $\text{Cl}^-$  stems from the erroneously large reduction of the polarizability of the  $\text{Cl}^-$  and its solvation shell.

In the PBE0-D3 simulations, there is a decrease in the average  $\text{Cl}^-$  polarizability (Table 4), thereby decreasing the response of the  $\text{Cl}^-$  charge density to perturbations induced by neighboring  $\text{H}_2\text{O}$  molecules (Fig. 9). While one would expect

**Table 4**  $\text{Cl}^-$  Polarizability and Hirshfeld-I Charge

Fraction of exact exchange	PZ	PBE	SCAN
$\text{Cl}^-$ Polarizability ( $\text{\AA}^3$ )			
0.00	7.27	4.31	4.13
0.05	6.93	4.21	4.05
0.10	6.47	4.15	3.99
0.15	6.03	4.07	3.93
0.20	5.63	3.99	3.85
0.25	5.34	3.92	3.79
Fraction of exact exchange			
$\text{Cl}^-$ Hirshfeld-I charge ( $e$ )			
0.00	0.06	-0.38	-0.41
0.05	0.03	-0.39	-0.41
0.10	0.00	-0.40	-0.41
0.15	-0.03	-0.40	-0.42
0.20	-0.06	-0.41	-0.42
0.25	-0.08	-0.41	-0.42

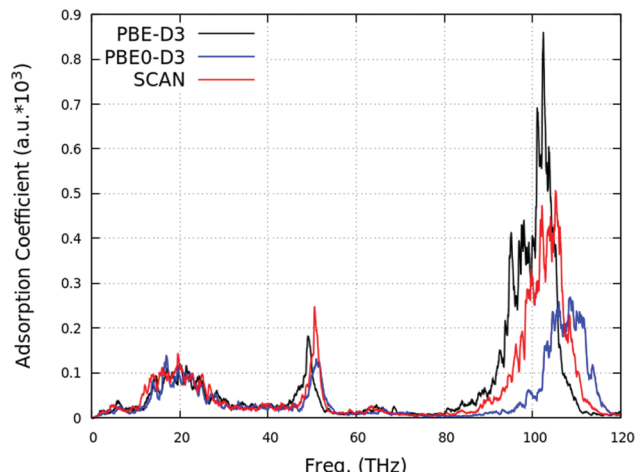


**Fig. 9** The infrared adsorption coefficient per unit length computed from the dipole moment of the  $\text{Cl}^-$  ion. The spectrum has been windowed using the Blackmann–Harris function<sup>75</sup> and smoothed with a Gaussian with a width of 15 fs.

the  $\text{Cl}^-$  H-bond lifetime to decrease upon adding a fraction of exact exchange, the reduction in the  $\text{Cl}^-$  polarizability leads to only a modest decrease in the lifetime (Table 2). This leads to a stiff  $\text{Cl}^-$  solvation shell and thus a more structured Cl-O RDF and a narrower distribution of Cl-O CNs compared to more accurate approximations (e.g. SCAN). Finally, it is thus interesting to note that, as one goes from PZ to PBE to SCAN, there is a reduction in the change in the polarizability and, to a lesser extent, the Hirshfeld-I charge as a function of the exact exchange fraction. This is important as the fundamental inability of DFT approximations to describe many electron systems means that the “best” functional for any application will likely include some fraction of exact exchange. However, when adding exact exchange to SCAN and likely other meta-GGA functionals, one is likely to see less of a reduction in polarizability compared to GGA functionals. Indeed, it has been shown that simply adding 0.25 exact exchange to SCAN does not necessarily improve its accuracy, and can even yield poorer performance than PBE-based hybrid functionals.<sup>46</sup> The exact exchange fraction of hybrid functionals therefore deserves careful consideration; while adding exact exchange causes modest changes in the energy and charge density, it also results in dramatic and at times erroneous changes in the response of the charge density.

## 4 Conclusion

AIMD simulations on a periodically replicated system of a single  $\text{Cl}^-$  solvated by  $63\text{H}_2\text{O}$  molecules have been carried out using the PBE-D3, PBE0-D3, and SCAN functionals to determine how different approximations of the exchange-correlation function impact the electronic properties and halide solvation structure. While the PBE0-D3 functional resulted in better agreement with experiment by reducing the structure of the O-O RDF, it still yielded slightly over-structured Cl-O and Cl-H RDFs, whereas the SCAN functional led to a significant reduction in the structure of the RDFs and superior agreement

with experiment. The discrepancy between PBE0-D3 and SCAN is explained by the large reduction in the  $\text{Cl}^-$  polarizability on the addition of exact exchange. This decrease in polarizability reduces the response of the  $\text{Cl}^-$  charge density to external perturbation, increasing the lifetime of  $\text{Cl}^-$  H-bond lifetimes, and thereby leading to a more rigid and structured solvation shell.

The present results emphasize the importance of careful consideration of appropriate functionals, as generally applicable and accurate hybrid functionals like PBE0-D3 can yield greater errors than their GGA counterparts in describing certain aspects of the system. In particular, the polarizability and charge of the LDA and GGA functionals tested, demonstrate a greater dependence on the fraction of exact exchange than the meta-GGA functional SCAN (Table 4). That said, the hybrid PBE0-D3 functional does yield more accurate results for the DOS, yielding a more accurate energy difference  $\delta E$  between the  $\text{Cl}^-(3p)$  band and  $\text{H}_2\text{O}(1b_1)$  band. While SCAN improved  $\delta E$ , it did not yield as large a  $\delta E$  as PBE0-D3, and a large portion of the  $\text{Cl}^-$  projected DOS is still within the VBM. Thus, while the addition of exact exchange helps to overcome fundamental limitations of DFT and generally improves the electronic structure, the fraction of exact exchange should be finely tuned and analyzed in order to prevent erroneous localization of the charge density and excessive reduction of the polarizability.

## Conflicts of interest

There are no conflicts to declare.

## Acknowledgements

This research includes calculations carried out on Temple University's HPC resources and thus was supported in part by the National Science Foundation through major research instrumentation Grant Number 1625061 and by the US Army Research Laboratory under Contract Number W911NF-16-2-0189. This research used resources of the National Energy Scientific Computing Center (NERSC), a U.S. Department of Energy Office of Science User Facility operated under No. DE-AC02-05CH11231. This work was supported by the Computational Chemical Center: Chemistry in Solution and at Interfaces funded by the DOE under Award No. DESC0019394.

## Notes and references

- 1 F. Hofmeister, *Arch. Exp. Pathol. Pharmakol.*, 1888, **24**, 247–260.
- 2 P. Lo Nstro and B. W. Ninham, *Chem. Rev.*, 2012, **112**, 2286–2322.
- 3 D. E. Draper, *Biophys. J.*, 2008, **95**, 5489–5495.
- 4 D. E. Draper, D. Grilley and A. M. Soto, *Annu. Rev. Biophys. Biomol. Struct.*, 2005, **34**, 221–243.
- 5 T.-M. Chang and L. X. Dang, *Chem. Rev.*, 2006, **106**, 1305–1322.
- 6 P. M. Dove, *Geochim. Cosmochim. Acta*, 1999, **63**, 3715–3727.
- 7 P. M. Dove and C. J. Nix, *Geochim. Cosmochim. Acta*, 1997, **61**, 3329–3340.
- 8 E. Ruiz-Agudo, M. Urosevic, C. V. Putnis, C. Rodríguez-Navarro, C. Cardell and A. Putnis, *Chem. Geol.*, 2011, **281**, 364–371.
- 9 A. D. Estilloré, H. S. Morris, V. W. Or, H. D. Lee, M. R. Alves, M. A. Marciano, O. Laskina, Z. Qin, A. V. Tivanski and V. H. Grassian, *Phys. Chem. Chem. Phys.*, 2017, **19**, 21101–21111.
- 10 A. P. Ault, T. L. Guasco, O. S. Ryder, J. Baltrusaitis, L. A. Cuadra-Rodriguez, D. B. Collins, M. J. Ruppel, T. H. Bertram, K. A. Prather and V. H. Grassian, *J. Am. Chem. Soc.*, 2013, **135**, 14528–14531.
- 11 P. J. DeMott, T. C. J. Hill, C. S. McCluskey, K. A. Prather, D. B. Collins, R. C. Sullivan, M. J. Ruppel, R. H. Mason, V. E. Irish, T. Lee, C. Y. Hwang, T. S. Rhee, J. R. Snider, G. R. McMeeking, S. Dhaniyala, E. R. Lewis, J. J. B. Wentzell, J. Abbott, C. Lee, C. M. Sultana, A. P. Ault, J. L. Axson, M. D. Martinez, I. Venero, G. Santos-Figueroa, M. D. Stokes, G. B. Deane, O. L. Mayol-Bracero, V. H. Grassian, T. H. Bertram, A. K. Bertram, B. F. Moffett and G. D. Franc, *Proc. Natl. Acad. Sci. U. S. A.*, 2016, **113**, 5797–5803.
- 12 K. A. Prather, T. H. Bertram, V. H. Grassian, G. B. Deane, M. D. Stokes, P. J. DeMott, L. I. Aluwihare, B. P. Palenik, F. Azam, J. H. Seinfeld, R. C. Moffet, M. J. Molina, C. D. Cappa, F. M. Geiger, G. C. Roberts, L. M. Russell, A. P. Ault, J. Baltrusaitis, D. B. Collins, C. E. Corrigan, L. A. Cuadra-Rodriguez, C. J. Ebbin, S. D. Forestieri, T. L. Guasco, S. P. Hersey, M. J. Kim, W. F. Lambert, R. L. Modini, W. Mui, B. E. Pedler, M. J. Ruppel, O. S. Ryder, N. G. Schoepp, R. C. Sullivan and D. Zhao, *Proc. Natl. Acad. Sci. U. S. A.*, 2013, **110**, 7550–7555.
- 13 L. Suo, O. Borodin, Y. Wang, X. Rong, W. Sun, X. Fan, S. Xu, M. A. Schroeder, A. V. Cresce, F. Wang, C. Yang, Y.-S. Hu, K. Xu and C. Wang, *Adv. Energy Mater.*, 2017, **7**, 1701189.
- 14 J. P. McEvoy and G. W. Brudvig, *Chem. Rev.*, 2006, **106**, 4455–4483.
- 15 A. C. Thenuwara, N. H. Attanayake, J. Yu, J. P. Perdew, E. J. Elzinga, Q. Yan and D. R. Strongin, *J. Phys. Chem. B*, 2018, **122**, 847–854.
- 16 M. J. DelloStritto, S. M. Piontek, M. L. Klein and E. Borguet, *J. Phys. Chem. Lett.*, 2019, **10**, 2031–2036.
- 17 D. Horinek and R. R. Netz, *Phys. Rev. Lett.*, 2007, **99**, 226104.
- 18 P. Jungwirth and D. J. Tobias, *J. Phys. Chem. B*, 2002, **106**, 6361–6373.
- 19 A. Tuladhar, S. M. Piontek, L. Frazer and E. Borguet, *J. Phys. Chem. C*, 2018, **122**, 12819–12830.
- 20 J. W. Schultz and D. F. Hornig, *J. Phys. Chem.*, 1961, **65**, 2131–2138.
- 21 W. M. Cox, J. H. Wolfenden and H. B. Hartley, *Proc. R. Soc. London, Ser. A*, 1934, **145**, 475–488.
- 22 G. Lamoureux and B. Roux, *J. Phys. Chem. B*, 2006, **110**, 3308–3322.
- 23 A. Grossfield, P. Ren and J. W. Ponder, *J. Am. Chem. Soc.*, 2003, **125**, 15671–15682.

- 24 L. Perera and M. L. Berkowitz, *J. Chem. Phys.*, 1991, **95**, 1954–1963.
- 25 F. Paesani, P. Bajaj and M. Riera, *Adv. Phys.: X*, 2019, **4**, 1631212.
- 26 J. E. Combariza, N. R. Kestner and J. Jortner, *J. Chem. Phys.*, 1994, **100**, 2851–2864.
- 27 S. S. Xantheas, *J. Chem. Phys.*, 1996, **100**, 9703–9713.
- 28 A. Bankura, B. Santra, R. A. DiStasio Jr., C. W. Swartz, M. L. Klein and X. Wu, *Mol. Phys.*, 2015, **113**, 2842–2854.
- 29 J. M. Heuft and E. J. Meijer, *J. Chem. Phys.*, 2003, **119**, 11788–11791.
- 30 P. Sałek, T. Helgaker, O. Vahtras, H. Ågren, D. Jonsson and J. Gauss, *Mol. Phys.*, 2005, **103**, 439–450.
- 31 J. Sun, A. Ruzsinszky and J. P. Perdew, *Phys. Rev. Lett.*, 2015, **115**, 036402.
- 32 J. Sun, R. C. Remsing, Y. Zhang, Z. Sun, A. Ruzsinszky, H. Peng, Z. Yang, A. Paul, U. Waghmare, X. Wu, M. L. Klein and J. P. Perdew, *Nat. Chem.*, 2016, **8**, 831–836.
- 33 P. R. Horn, Y. Mao and M. Head-Gordon, *Phys. Chem. Chem. Phys.*, 2016, **18**, 23067–23079.
- 34 B. B. Bizzarro, C. K. Egan and F. Paesani, *J. Chem. Theory Comput.*, 2019, **15**, 2983–2995.
- 35 C. Zhang, T. A. Pham, F. Gygi and G. Galli, *J. Chem. Phys.*, 2013, **138**, 181102.
- 36 A. P. Gaiduk and G. Galli, *J. Phys. Chem. Lett.*, 2017, **8**, 1496–1502.
- 37 A. K. Soper and K. Weckström, *Biophys. Chem.*, 2006, **124**, 180–191.
- 38 R. Mancinelli, A. Botti, F. Bruni, M. A. Ricci and A. K. Soper, *J. Phys. Chem. B*, 2007, **111**, 13570–13577.
- 39 Y. Chen, H. I. Okur, N. Gomopoulos, C. Macias-Romero, P. S. Cremer, P. B. Petersen, G. Tocci, D. M. Wilkins, C. Liang, M. Ceriotti and S. Roke, *Sci. Adv.*, 2016, **2**, e1501891.
- 40 A. W. Omta, M. F. Kropman, S. Woutersen and H. J. Bakker, *Science*, 2003, **301**, 347–349.
- 41 L.-A. k. Näslund, D. C. Edwards, P. Wernet, U. Bergmann, H. Ogasawara, L. G. M. Pettersson, S. Myneni and A. Nilsson, *J. Phys. Chem. A*, 2005, **109**, 5995–6002.
- 42 I. Juurinen, T. Pykkänen, K. O. Ruotsalainen, C. J. Sahle, G. Monaco, K. Hämäläinen, S. Huotari and M. Hakala, *J. Phys. Chem. B*, 2013, **117**, 16506–16511.
- 43 M. Chen, H.-Y. Ko, R. C. Remsing, M. F. C. Andrade, B. Santra, Z. Sun, A. Selloni, R. Car, M. L. Klein, J. P. Perdew and X. Wu, *Proc. Natl. Acad. Sci. U. S. A.*, 2017, **114**, 10846–10851.
- 44 T. Duignan, G. K. Schenter, J. Fulton, T. Huthwelker, M. Balasubramanian, M. Galib, M. D. Baer, J. Wilhelm, J. Hutter, M. D. Ben, X. S. Zhao and C. J. Mundy, *Phys. Chem. Chem. Phys.*, 2019, DOI: 10.1039/C9CP05610F.
- 45 J. Wiktor, F. Ambrosio and A. Pasquarello, *J. Chem. Phys.*, 2017, **147**, 216101.
- 46 K. Hui and J.-D. Chai, *J. Chem. Phys.*, 2016, **144**, 044114.
- 47 R. Mancinelli, A. Botti, F. Bruni, M. A. Ricci and A. K. Soper, *Phys. Chem. Chem. Phys.*, 2007, **9**, 2959–2967.
- 48 A. P. Gaiduk, M. Govoni, R. Seidel, J. H. Skone, B. Winter and G. Galli, *J. Am. Chem. Soc.*, 2016, **138**, 6912–6915.
- 49 H. J. C. Berendsen, J. R. Grigera and T. P. Straatsma, *J. Chem. Phys.*, 1987, **91**, 6269–6271.
- 50 S. Plimpton, *J. Comput. Phys.*, 1995, **117**, 1–19.
- 51 L. Martínez, R. Andrade, E. G. Birgin and J. M. Martínez, *J. Comput. Chem.*, 2009, **30**, 2157–2164.
- 52 J. VandeVondele, M. Krack, F. Mohamed, M. Parrinello, T. Chassaing and J. Hutter, *Comput. Phys. Commun.*, 2005, **167**, 103–128.
- 53 J. P. Perdew, K. Burke and M. Ernzerhof, *Phys. Rev. Lett.*, 1996, **77**, 3865–3868.
- 54 J. P. Perdew, K. Burke and M. Ernzerhof, *Phys. Rev. Lett.*, 1997, **78**, 1396.
- 55 S. Grimme, *J. Comput. Chem.*, 2006, **27**, 1787–1799.
- 56 S. Grimme, J. Antony, S. Ehrlich and H. Krieg, *J. Chem. Phys.*, 2010, **132**, 154104.
- 57 S. Grimme, S. Ehrlich and L. Goerigk, *J. Comput. Chem.*, 2011, **32**, 1456–1465.
- 58 C. Adamo and V. Barone, *J. Chem. Phys.*, 1999, **110**, 6158–6170.
- 59 S. Goedecker, M. Teter and J. Hutter, *Phys. Rev. B: Condens. Matter Mater. Phys.*, 1996, **54**, 1703–1710.
- 60 J. VandeVondele and J. Hutter, *J. Chem. Phys.*, 2007, **127**, 114105.
- 61 Y. Yao and Y. Kanai, *J. Chem. Theory Comput.*, 2018, **14**, 884–893.
- 62 G. Miceli, J. Hutter and A. Pasquarello, *J. Chem. Theory Comput.*, 2016, **12**, 3456–3462.
- 63 M. Guidon, J. Hutter and J. VandeVondele, *J. Chem. Theory Comput.*, 2010, **6**, 2348–2364.
- 64 P. Giannozzi, S. Baroni, N. Bonini, M. Calandra, R. Car, C. Cavazzoni, D. Ceresoli, G. L. Chiarotti, M. Cococcioni, I. Dabo, A. D. Corso, S. D. Gironcoli, S. Fabris, G. Fratesi, R. Gebauer, U. Gerstmann, C. Gougaussis, Anton Kokalj, M. Lazzeri, L. Martin-Samos, N. Marzari, F. Mauri, R. Mazzarello, S. Paolini, A. Pasquarello, L. Paulatto, C. Sbraccia, S. Scandolo, G. Sclauzero, A. P. Seitsonen, A. Smogunov, P. Umari and R. M. Wentzcovitch, *J. Phys.: Condens. Matter*, 2009, **21**, 395502.
- 65 P. Giannozzi, O. Andreussi, T. Brumme, O. Bunau, M. B. Nardelli, M. Calandra, R. Car, C. Cavazzoni, D. Ceresoli, M. Cococcioni, N. Colonna, I. Carnimeo, A. D. Corso, S. D. Gironcoli, P. Delugas, R. A. DiStasio Jr., A. Ferretti, A. Floris, G. Fratesi, G. Fugallo, R. Gebauer, U. Gerstmann, F. Giustino, T. Gorni, J. Jia, M. Kawamura, H.-Y. Ko, A. Kokalj, E. Küçükbenli, M. Lazzeri, M. Marsili, N. Marzari, F. Mauri, N. L. Nguyen, H.-V. Nguyen, A. Otero-de-la-Roza, L. Paulatto, S. Poncé, D. Rocca, R. Sabatini, B. Santra, M. Schlipf, A. P. Seitsonen, A. Smogunov, I. Timrov, T. Thonhauser, P. Umari, N. Vast, X. Wu and S. Baroni, *J. Phys.: Condens. Matter*, 2017, **29**, 465901.
- 66 D. R. Hamann, M. Schlüter and C. Chiang, *Phys. Rev. Lett.*, 1979, **43**, 1494–1497.
- 67 F. L. Hirshfeld, *Theor. Chim. Acta*, 1977, **44**, 129–138.
- 68 P. Bultinck, C. Van Alsenoy, P. W. Ayers and R. Carbó-Dorca, *J. Chem. Phys.*, 2007, **126**, 144111.
- 69 J. A. Morrone and R. Car, *Phys. Rev. Lett.*, 2008, **101**, 017801.

- 70 Y. Marcus, *Chem. Rev.*, 2009, **109**, 1346–1370.
- 71 B. Winter, R. Weber, W. Widdra, M. Dittmar, M. Faubel and I. V. Hertel, *J. Phys. Chem. A*, 2004, **108**, 2625–2632.
- 72 B. Winter, R. Weber, I. V. Hertel, M. Faubel, P. Jungwirth, E. C. Brown and S. E. Bradforth, *J. Am. Chem. Soc.*, 2005, **127**, 7203–7214.
- 73 M. Masia, *J. Phys. Chem. A*, 2013, **117**, 3221–3226.
- 74 R. Ramírez, T. López-Ciudad, P. Kumar and D. Marx, *J. Chem. Phys.*, 2004, **121**, 3973–3983.
- 75 F. J. Harris, *Proc. IEEE*, 1978, **66**, 51–83.
- 76 J. P. Perdew and A. Zunger, *Phys. Rev. B: Condens. Matter Mater. Phys.*, 1981, **23**, 5048–5079.